Orbital parameters of infalling satellite haloes in the hierarchical ΛCDM model

Lilian Jiang,[*] Shaun Cole, Till Sawala and Carlos S. Frenk

Institute for Computational Cosmology, Department of Physics, University of Durham, South Road, Durham DH1 3LE, UK

ABSTRACT

We present distributions of orbital parameters of infalling satellites of Λ cold dark matter (ΛCDM) haloes in the mass range 10^{12}–10^{14} $M_\odot$, which represent the initial conditions for the subsequent evolution of substructures within the host halo. We use merger trees constructed in a high-resolution cosmological *N*-body simulation to trace satellite haloes, and identify the time of infall. We find significant trends in the distribution of orbital parameters with both the host halo mass and the ratio of satellite-to-host halo masses. For all host halo masses, satellites whose infall mass is a larger fraction of the host halo mass have more eccentric, radially biased orbits. At fixed satellite-to-host halo mass ratio, high-mass haloes are biased towards accreting satellites on slightly more radial orbits. To characterize the orbital distributions fully requires fitting the correlated bivariate distribution of two chosen orbital parameters (e.g. radial and tangential velocity or energy and angular momentum). We provide simple fits to one choice of the bivariate distributions, which when transformed faithfully, captures the behaviour of any of the projected one-dimensional distributions.

Key words: methods: numerical – galaxies: haloes – cosmology: theory – dark matter.

1 INTRODUCTION

In the current cosmological structure formation model, dark matter haloes grow by the merging of smaller systems (White & Rees 1978; Davis et al. 1985), leading to hierarchical halo growth. Substructures that are accreted on to a host halo can survive for significant periods of time within the host halo (Chandrasekhar 1943; Klypin et al. 1999; Moore et al. 1999; Binney & Tremaine 2008; Boylan-Kolchin, Ma & Quataert 2008; Jiang et al. 2008). These substructures can host satellite galaxies, such as those found in the Local Group, and galaxy clusters. Thus, it is important to study the distribution of the initial orbital parameters of subhaloes at the time of infall as they represent the initial conditions which determine the later evolution of the substructures in their host haloes.

Semi-analytic models of galaxy formation rely on prescriptions for dynamical friction survival times and tidal stripping (see Baugh 2006 for a review). Assuming the halo potential to be spherically symmetric, a satellite orbit can be defined by the plane of the orbit and two further parameters related to the energy and angular momentum such as circularity and pericentre. Previous authors have studied the distributions of such orbital parameters for substructures in numerical simulations (Tormen 1997; Vitvitska et al. 2002; Benson 2005; Wang et al. 2005; Zentner et al. 2005; Khochfar & Burkert 2006; Wetzel 2011). Tormen (1997) investigated the infall of satellites into the haloes of galaxy cluster mass, and reported that

more massive satellites move along slightly more eccentric orbits, with lower specific angular momentum and smaller pericentres. Benson (2005) presented evidence for a satellite mass dependence of the distribution of orbital parameters, but was unable to characterize these trends accurately due to the limited statistics. Apparently in slight contradiction, Wetzel (2011) reports that the orbital parameters do not significantly depend on the satellite halo mass but depend more on the host halo mass. These studies were hampered by limited dynamic range and sample size. The high resolution and large volume of the simulation we analyse allow us to quantify trends in both satellite and host halo mass.

The two parameters characterizing a satellite orbit are, in general, correlated. Wetzel (2011) provides fits to circularity and pericentre, but he stopped short of examining correlations between these parameters which are important if one wants to select representative orbits from the distribution. Khochfar & Burkert (2006) found a tight correlation between pericentre and circularity. Tormen (1997), Gill et al. (2004) and Benson (2005) also find correlations between orbital parameters.

In this paper, we investigate the correlations between different possible pairs of parameters. We show that to a good approximation total infall velocity and the fraction of this velocity which is in the radial direction are uncorrelated. We present fits to these and show that when transformed these fits provide accurate descriptions of the distributions of other choices of orbital parameters.

Most previous work has focused on orbits only at redshift $z = 0$, or on the satellites that are still identified at $z = 0$. In our work, we focus on host haloes that exist at $z = 0$, but we analyse the orbits of

all satellites that fall into the host halo after its formation (defined as when its main progenitor had half the final halo mass), regardless of whether the satellite is still identifiable at $z = 0$.

Our paper is structured as follows. In Section 2, we briefly outline the methods including a detailed description of the N-body simulation, the identification of halo mergers and the measurement of orbital parameters. In Section 3, we present detailed analysis of the orbital parameters. We conclude in Section 4.

2 METHODS

2.1 Simulation

Our analysis is based on the DOVE simulation, a Λ cold dark matter(ΛCDM) cosmological dark matter only simulation of a periodic volume with side length 100 Mpc, with cosmological parameters adapted from the *WMAP7* analysis of Komatsu et al. (2011). The Hubble parameter, density parameter, cosmological constant, scalar spectral index and linear rms mass fluctuation in 8 h^{-1}Mpc radius spheres were $H_0 = 70.4 \, \mathrm{km \, s^{-1}}$, $\Omega_m = 0.272$, $\Omega_\Lambda = 0.728$, $n_s = 0.97$ and $\sigma_8 = 0.81$, respectively. The dark matter is represented by $N_p = 1620^3$ particles of mass $m_p = 8.8 \times 10^6 \, \mathrm{M}_\odot$. Initial conditions were set up using second-order Lagrangian perturbation theory (Jenkins 2010), with phases set using the multiscale Gaussian white noise field *Panphasia* (Jenkins 2013). These phases were chosen to be the same as in the EAGLE simulation (Schaye et al. 2014) and are fully specified by the *Panphasia* descriptor [Panph1,L16,(31250,23438,39063),S12,CH1050187043, EAGLE_L0100_VOL1]. The initial conditions were evolved to $z = 0$ using the GADGET-3 N-body code, which is an enhanced version of the code described in Springel (2005).

The particle positions and velocities were output at 160 snapshots, equally spaced in log (a) from $z = 20$. At each output, haloes were identified using a Friends-of-Friends algorithm (FOF; Davis et al. 1985), and the SUBFIND algorithm (Springel et al. 2001) was used to identify self-bound substructures ('subhaloes') within them. We define our FOF haloes by the conventional linking length parameter of $b = 0.2$ (the linking length is defined as b times the mean interparticle separation). Typically, the main SUBFIND subhalo contains most of the mass of the original FOF halo, only unbound particles and those bound to secondary subhaloes are excluded. We keep all haloes and subhaloes with more than 20 particles, corresponding to $2 \times 10^8 \, \mathrm{M}_\odot$.

2.2 Orbital parameters

We define the virial mass, M_vir, and associated virial radius, r_vir, of a dark matter halo using a simple spherical overdensity criterion centred on the potential minimum:

$$M_\mathrm{vir} = \frac{4}{3}\pi \Delta \, \rho_\mathrm{crit} \, r_\mathrm{vir}^3, \tag{1}$$

where ρ_crit is the cosmological critical density and Δ is the specified overdensity. We adopt $\Delta = 200$ and include all the particles inside this spherical volume, not only the particles grouped by the adopted halo finder, to define the enclosed mass, M_{200}, and associated radius r_{200}. This choice of $\Delta = 200$ is largely a matter of convention, but has been shown roughly to correspond to the boundary at which the haloes are in approximate dynamical equilibrium (e.g. Cole & Lacey 1996). We express velocities in units of the virial velocity, V_{200}, of the host halo.

For a spherical potential, the orbit of a satellite can be fully specified by the orientation of the orbit and two non-trivial parameters related to its energy, E, and the modulus of its angular momentum, J. There are various choices for these two parameters. The choice made by Benson (2005) and others of the radial, V_r, and tangential, V_θ, velocities at infall benefits from being directly measurable quantities and being simple. In contrast, Tormen (1997) adopted the *circularity*, defined as the total angular momentum in units of the angular momentum for a circular orbit of the same energy, $J/J_\mathrm{circ}(E)$, and the infall radius in units of the radius of a circular orbit of the same energy, $r/r_\mathrm{circ}(E)$. These have the advantage of depending only on the conserved quantities E and J (Note, the r here is the radius at infall and so equals r_{200} in our study.), but require adopting a model of the halo potential. The particular form of these two parameters is motivated by theoretical modelling including that of satellite orbital decay due to dynamical friction (Lacey & Cole 1993; Jiang et al. 2008). To define these two parameters, we adopt a singular isothermal sphere (SIS; Cole & Lacey 1996) as a simple model for the density profile of dark matter haloes. This choice is consistent with assumptions in Lacey & Cole (1993), and so provides orbital parameters that can be directly substituted into their merger time formula. In Section 3.5, we also provide formulae for computing the corresponding orbital parameters if one instead adopts a more realistic NFW potential (Navarro, Frenk & White 1996).

Here, we derive the transformations between these two parametrization. Defining the zero-point of the gravitational potential to be at r_{200}, where the circular velocity, V_{200}, is given by $V_{200} = \sqrt{GM_{200}/r_{200}}$, we can express the gravitational potential as

$$\phi(r) = V_{200}^2 \ln(r/r_{200}). \tag{2}$$

Thus, for a satellite crossing r_{200} with radial and tangential velocities, V_r and V_θ, the total energy per unit mass is

$$E = \frac{1}{2}\left(V_r^2 + V_\theta^2\right). \tag{3}$$

As the circular velocity is constant for a SIS, the radius, of a circular orbit of the same energy is given by

$$\frac{1}{2}\left(V_r^2 + V_\theta^2\right) = \frac{1}{2}V_{200}^2 + V_{200}^2 \ln(r_\mathrm{circ}/r_{200}), \tag{4}$$

implying

$$\frac{r_\mathrm{circ}(E)}{r_{200}} = \exp\left(\frac{V_r^2 + V_\theta^2 - V_{200}^2}{2V_{200}^2}\right). \tag{5}$$

As the corresponding angular momentum of a circular orbit is $J_\mathrm{circ}(E) = M_s V_{200} r_\mathrm{circ}(E)$, we have

$$\frac{J}{J_\mathrm{circ}(E)} = \frac{V_\theta}{V_{200}}\exp\left(-\frac{V_r^2 + V_\theta^2 - V_{200}^2}{2V_{200}^2}\right). \tag{6}$$

Another useful quantity to define is the composite parameter

$$\Theta = \left(\frac{J}{J_\mathrm{circ}(E)}\right)^{0.78}\left(\frac{r_{200}}{r_\mathrm{circ}(E)}\right)^2. \tag{7}$$

Its utility is that Lacey & Cole (1993) showed that the orbital decay time of a satellite of mass M_s due to dynamical friction within a host halo of mass M_h is given by

$$\tau_\mathrm{mrg} = \Theta \, \tau_\mathrm{dyn} \frac{0.3722}{\ln(\Lambda_\mathrm{coulomb})}\frac{M_h}{M_s}, \tag{8}$$

where τ_dyn is the dynamical time of the host halo and $\ln(\Lambda_\mathrm{coulomb})$ is taken to be $\ln(M_h/M_s)$. This formula assumes that the satellite can be treated as a point mass orbiting in a host halo with a SIS

density profile and is valid when $\tau_{\mathrm{mrg}} \gg \tau_{\mathrm{dyn}}$. In this model, it is only necessary to know the one-dimensional distribution of Θ values rather than the bivariate distribution of, say, V_r and V_θ to determine the distribution of orbital decay times.

2.3 Identifying halo mergers

We follow the evolution, infall and merging of haloes and subhaloes using merger trees. Our starting point is the catalogue of FOF haloes and their constituent subhaloes at redshift zero. We build subhalo merger trees linking each subhalo to its progenitors and descendants using the algorithm described in appendix A2 of Jiang et al. (2014). Next, we identify both the progenitors of the FOF haloes and the subhaloes which fall into them. For each FOF halo, we trace its progenitor in the previous snapshot by identifying the main progenitor of its main subhalo. We then define the virial radius of this progenitor halo such that a sphere of this radius centred on the particle at the potential minimum of the main subhalo encloses 200 times the critical density as defined in equation (1). We trace the main progenitor of each redshift zero FOF halo back in this way until the last snapshot at which its mass is greater than half the final halo mass. We choose not to consider mergers before the formation time of the main halo as we bin our results by the halo mass at $z = 0$ and wish this to select (within a factor of 2) the mass of the main halo when the merger takes place. To identify subhaloes that merge on to this main halo progenitor we not only trace the progenitors of subhaloes that are in the halo at redshift zero, but also those that were inside progenitors of the main halo at some point but which have since been disrupted, merged or escaped. Hence, we trace every individual subhalo from its formation redshift to the redshift when it first crosses the virial radius of the host halo.

In order to find the precise crossing time, we save the orbital information from the snapshots just before and after a satellite subhalo crosses the virial radius. Then, we interpolate both the satellite position (relative to the halo centre) and the halo virial radius linearly to find the time when the subhalo first crosses the virial radius. To investigate the accuracy of the interpolation scheme, we considered two methods of interpolating the satellite orbital parameters to this crossing time.

(i) We interpolate the energy (using the SIS approximation of the halo potential described in Section 2.2) and angular momentum linearly in redshift to the crossing time. We then compute other orbital parameters such as the radial and tangential velocities from this interpolated energy and angular momentum.

(ii) Alternatively, we interpolate each component of the satellite's velocity linearly in redshift to the crossing time and then compute the required orbital parameters from the interpolated velocity and position.

Provided that our simulation snapshots are sufficiently closely spaced, we would expect these two methods to give very similar results. This is indeed what we find as demonstrated in Fig. 1 which compares the distribution of the various orbital parameters for satellites satisfying $M_s/M_h > 0.05$ at the time of infall in our full sample of haloes. Throughout the rest of this paper, we show results just from the method that linearly interpolates the energy and angular momentum. We would expect this to be the more accurate method as these two quantities are almost conserved and so only vary slowly with the interpolation parameter.

Accurately defining the orbital parameters at the crossing time is an important issue that has been considered in earlier work. The
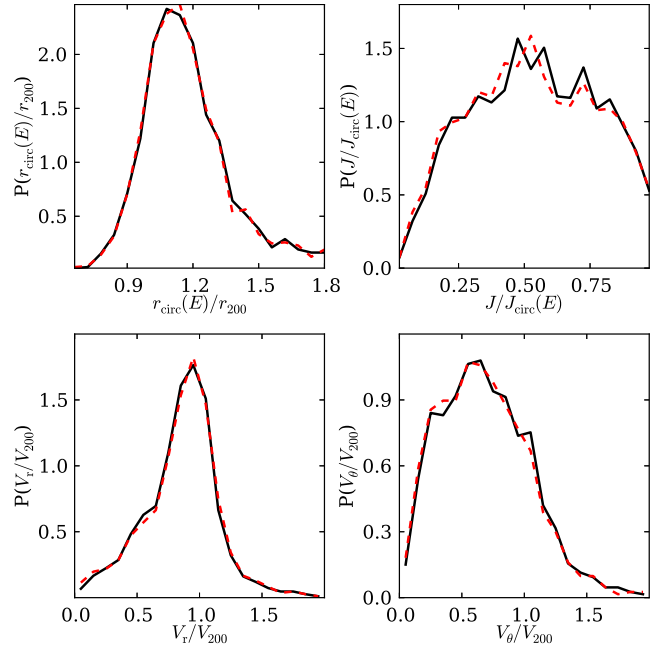

Figure 1. Tests of the interpolation scheme on the distributions of the orbital parameters $r_{\mathrm{circ}}(E)/r_{200}$, $J/J_{\mathrm{circ}}(E)$, V_r/V_{200} and V_θ/V_{200}. The panel shows the differential distribution of orbital parameters in the mass ratio bin: $M_s/M_h > 0.05$ for all the host haloes in our sample. Solid lines show the results using linear interpolation of energy and angular momentum, dotted lines show results using linear interpolation of velocity and position.

approach adopted by Benson (2005) and Vitvitska et al. (2002) was to search for pairs of haloes within some separation r_{max} which are about to merge and then predict their crossing time by modelling them as two isolated point masses. A similar approach was taken by Tormen (1997), Khochfar & Burkert (2006) and Wetzel (2011). When using such schemes one must apply a weighting to correct for the underrepresentation of satellites with large infall velocities, some of which will be at separations greater than r_{max} at the earlier snapshot. In our work, due to the higher time resolution of our simulation outputs, we do not have to limit the separation between satellite and host halo at the snapshot prior to infall and instead form a complete census of all the infalling satellites.

2.4 Formation and infall redshifts

As we want our measured orbital parameter distributions to be directly applicable to semi-analytic galaxy formation models, we trace all the infalling subhaloes back to the formation time of the main halo, where its formation time is defined as when its main progenitor has half the final, $z = 0$, halo mass. We bin our halo samples by their mass at redshift $z = 0$ and so by not tracing haloes back further in time; we avoid significant ambiguity in the mass of the main halo at the time satellites are accreted, i.e. at all infall events the main halo is always within a factor of 2 the final halo mass. The probability distribution function of halo formation redshifts, z_{HF}, (normalized such that the integral over the distribution is unity) are shown in the top row of Fig. 2 for each of our final halo mass bins. As expected we see that lower mass haloes form earlier. The median formation redshift of our 10^{12}, 10^{13} and 10^{14} M$_\odot$ haloes are 1.14, 0.92 and 0.66, respectively.
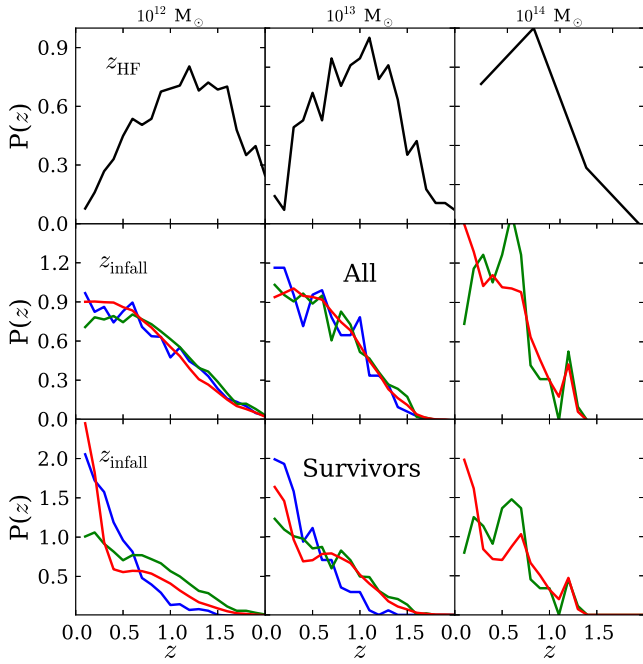
Figure 2. The distributions of halo formation redshifts and the redshifts at which satellites fall into these haloes. Each column is for a fixed final halo mass as labelled at the top of the figure. The top row is the distribution of halo formation redshifts. The middle row is the distribution of satellite infall redshifts for all infalling satellites, while bottom row is for the subset of these satellites which survive as subhaloes at $z = 0$. In the bottom two rows the line colour indicates the satellite-to-host mass ratio. The red lines are for $0.0001 < M_s/M_h < 0.005$, green for $0.005 < M_s/M_h < 0.05$ and blue for $M_s/M_h > 0.05$.

The middle row of Fig. 2 shows the distribution of infall redshifts, z_{infall}, split both by final halo mass and by the ratio of satellite-to-host mass at infall. These distributions rise steadily towards redshift $z = 0$ (though the distributions for the highest mass bin are noisy because of the limited size of that sample) from the upper redshift set by when the first haloes in the sample form. The most interesting aspect is that infall redshift distribution at fixed halo mass is essentially independent of satellite-to-host mass ratio. This is equivalent to the mass distribution of the infalling satellites, measured in units of the host halo mass, being independent of redshift. Given that the distribution of host halo masses is constrained not to vary greatly with redshift (only haloes with mass greater than half the final mass are retained in the sample) then this behaviour is expected in simple excursion set models of hierarchical growth (Lacey & Cole 1993).

The bottom row of Fig. 2 also shows distributions of infall redshifts, but now just for the satellites that survive and are identifiable at redshift $z = 0$. The median redshifts of these distributions are compared to those of corresponding complete samples in Table 1. Comparing these values and the distributions shown in the bottom and middle rows of Fig. 2, one clearly sees that the typical infall redshift of surviving satellites is significantly lower than that of the complete sample.

This is, at least in part, a resolution effect as we are unable to identify satellites with fewer than 20 particles. Thus, the shift to lower infall redshifts is greatest for the lowest mass satellites which are the ones with the smaller satellite-to-host mass ratio in the lower halo mass bins.

3 ORBITAL PARAMETER DISTRIBUTIONS

3.1 Comparison to previous work

Fig. 3 compares our orbital parameter distributions with those from Tormen (1997), Benson (2005) and Wetzel (2011). In all panels, the black solid lines show the distributions for satellites with mass ratios in the range $0.05 < M_s/M_h < 0.5$ averaged over all our analysed haloes which span the mass range $5 \times 10^{11} < M_h < 2.5 \times 10^{14}$ M$_\odot$. In general, our results are in good agreement with these published data sets and those of Wang et al. (2005), Zentner et al. (2005) and Khochfar & Burkert (2006) despite variations between these studies in the definition of crossing time and the choice of cosmology.

The selection of Tormen (1997) data which we plot matches the $M_s/M_h > 0.05$[1] cut used in our own data, but is for host haloes with typical masses of 10^{15} M$_\odot$. The good agreement we find with Tormen (1997) is only expected if, as we find below, the distributions depend only weakly on halo mass at fixed M_s/M_h. The Benson (2005) data are based on a wide range of simulations of different volumes and resolutions. In this sample, he uses all satellites and haloes with masses greater than 10^{11} M$_\odot$ and states that the typical ratio $M_s/M_h = 0.08$. The smooth radial and tangential velocity distributions we plot in the lower panels of Fig. 3 are the fitted distributions presented by Benson (2005). Benson (2005) and also Vitvitska et al. (2002) modelled the radial distribution as a Gaussian and the tangential distribution as a Rayleigh or 2D Maxwell–Boltzmann distribution. The agreement with our results is reasonable. The radial and tangential velocity distributions of Wetzel (2011) are in very good agreement with our results. Like Benson, Wetzel uses all satellites and haloes above a fixed mass cut, 10^{10} M$_\odot$, and so we would expect the mean M_s/M_h ratio to be similar to that of Benson and to our $0.05 < M_s/M_h < 0.5$ sample. The comparison of $J/J_{circ}(E)$ distributions between us and Wetzel is not strictly fair as we compute $J_{circ}(E)$ using the SIS model while he models the satellite and host as two point masses. However while this introduces a bias for satellites for which $M_s/M_h \ll 1$, we find that the resulting distributions are very similar for satellites with $0.05 < M_s/M_h < 0.5$ (see Appendix A).

3.2 Orbital parameters: mass ratio and mass dependence

Fig 4 presents our results for the orbital parameter distributions for three bins of halo mass and three bins of satellite-to-host halo mass ratio. We reiterate that the host halo mass bins are defined by the mass of the host haloes at $z = 0$ while the mass ratio, M_s/M_h, is defined by the values at the infall redshift.

The top two rows of Fig. 4 show the distributions of radial and tangential velocities at infall. The radial distributions peak close $V_r = V_{200}$ and the tangential distributions at a lower value of around $V_\theta = 0.65 V_{200}$. As very few satellites are on unbound orbits, both distributions only have small tails beyond $1.5 V_{200}$. Independently of host halo mass, we see that the distributions of radial velocities become broader for lower mass satellites with little change in the location of the peak of the distribution. In contrast for the tangential velocities the mode of the distribution shifts to higher values for less massive satellites. The most massive satellites are on the most radial, low angular momentum, orbits. The dependence of these distributions on halo mass at fixed M_s/M_h is much weaker. This can be seen in the right-hand panels where, to a first approximation,

---

[1] We were able to apply this cut as G. Tormen kindly supplied his catalogue of satellite orbital parameters in electronic form.

Table 1. The median values of infall redshifts for both all and surviving subhaloes and the orbital parameter, $\log_{10} \Theta$ for bins of final halo mass, M_h, and the satellite-to-host mass ratio at infall, M_s/M_h. The errors were estimated by bootstrap resampling of the halo sample.

M_h	M_s/M_h	$\log_{10} \Theta$	z_{infall} survivors	z_{infall} all
10^{12} M$_\odot$	0.0001–0.005	0.076 ± 0.002	0.217 ± 0.006	0.491 ± 0.007
10^{13} M$_\odot$	0.0001–0.005	0.051 ± 0.004	0.428 ± 0.025	0.516 ± 0.017
10^{14} M$_\odot$	0.0001–0.005	0.050 ± 0.017	0.380 ± 0.064	0.409 ± 0.053
10^{12} M$_\odot$	0.005–0.05	0.027 ± 0.003	0.462 ± 0.009	0.521 ± 0.010
10^{13} M$_\odot$	0.005–0.05	-0.009 ± 0.012	0.480 ± 0.024	0.522 ± 0.022
10^{14} M$_\odot$	0.005–0.05	-0.015 ± 0.047	0.483 ± 0.086	0.483 ± 0.062
10^{12} M$_\odot$	0.05–0.5	-0.082 ± 0.007	0.290 ± 0.012	0.511 ± 0.019
10^{13} M$_\odot$	0.05–0.5	-0.130 ± 0.021	0.268 ± 0.031	0.484 ± 0.040
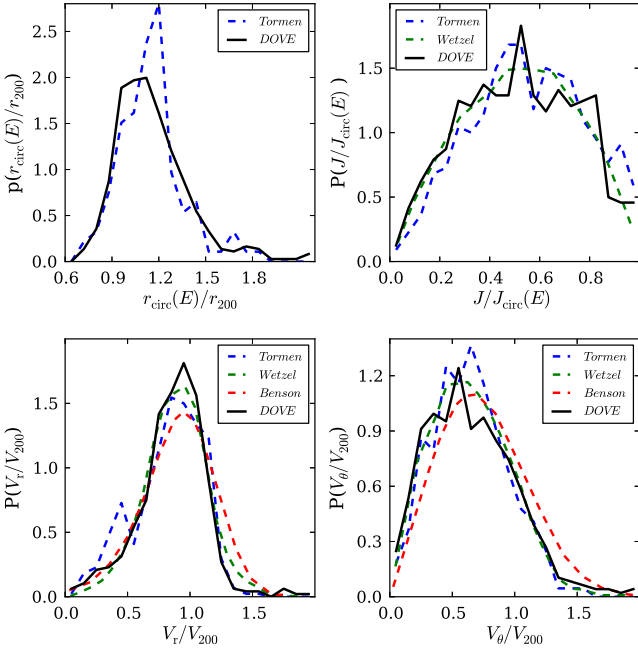
Figure 3. Comparison to published distributions of the orbital parameters $r_{circ}(E)/r_{200}$, $J/J_{circ}(E)$, V_r/V_{200} and V_θ/V_{200}. In all the panels, the black solid line shows the distribution of the satellite orbital parameters for infalling satellites in our analysed host haloes (covering the mass range 5×10^{11}–2.5×10^{14} M$_\odot$) with satellite-to-host halo mass ratios spanning 0.05–0.5. This range is typical of that probed by the samples to which we are comparing. Blue, green and red dashed lines show the results from the work of Tormen (1997), Wetzel (2011) and Benson (2005), respectively.

the lines of the same colour (same M_s/M_h) coincide. There is some residual dependence on halo mass (different line styles), with orbits becoming more radial – the V_θ/V_{200} distributions peaking at lower values – for more massive haloes, but this trend is much weaker.

The middle row of Fig. 4 shows the distributions of circularity, $J/J_{circ}(E)$. The distributions are broad with those for the $M_s/M_h > 0.05$ bin peaking at close to a circularity of a half. In each bin of halo mass, we again see the trend, for higher mass satellites to have less circular, more radially biased orbits. Also, once again, the trends with satellite-to-halo mass ratio are much stronger than those with halo mass.

The penultimate row of Fig. 4 shows the distributions of $r_{circ}(E)/r_{200}$. This is essentially a measure of the energies of the orbits, with higher $r_{circ}(E)/r_{200}$ corresponding to less bound orbits. At each halo mass, there is a strong trend for the more massive

satellites to be more strongly bound. Again, the variations of the distributions with halo mass, at fixed satellite-to-halo mass ratio, are much weaker.

These trends are consistent with the picture put forward by Libeskind et al. (2005) that within the filaments of the cosmic web that surround an accreting dark matter halo, the most massive infalling haloes move along the central spines of the filaments. In this way, the filamentary structures act as focusing rails which direct massive satellites on to predominantly radial orbits. Perhaps more simply, the force on the most massive satellites is dominated by the central halo while lower mass satellites can be significantly perturbed by other more massive satellites.

We show the distribution of the composite orbital parameter Θ in the bottom row of Fig. 4 and list their median values in Table 1. We see a clear shift in the distributions towards higher values of Θ with decreasing values of M_s/M_h and negligible dependence on host halo mass. According to equation (8) this will contribute to lower mass satellites having longer merger time-scales, but this effect is subdominant to the explicit M_h/M_s term in that equation which also acts in the same sense.
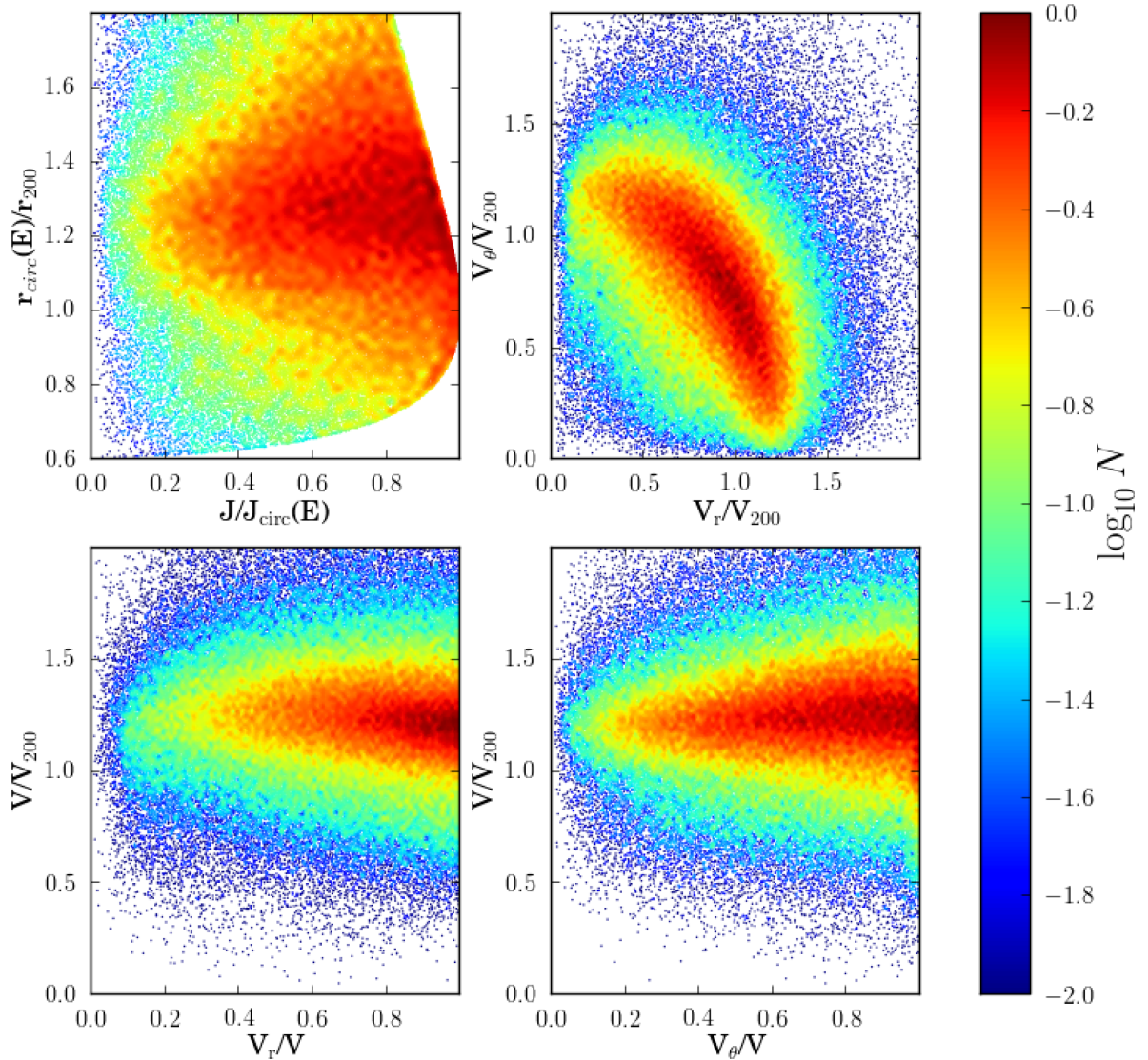
3.3 2D distribution of orbital parameters

As described in the Benson (2005) paper, the radial and tangential velocity distributions are tightly correlated. Consequently the one-dimensional distributions presented in Fig. 4 are not a sufficient characterization of the orbital parameter distributions. We emphasize this in Fig. 5 which shows bivariate distributions of various orbital parameter combinations.

The top-left panel of Fig. 5 shows the bivariate distribution of $r_{circ}(E)/r_{200}$ and $J/J_{circ}(E)$. The first thing to note in this distribution is that there are excluded regions at high value of $J/J_{circ}(E)$ both for low and high values of $r_{circ}(E)/r_{200}$. These arise from our stipulation that we are characterizing the orbits of satellites when they first cross r_{200}. The plotted distribution touches the right-hand axis at $r_{circ}(E)/r_{200} = 1$ and $J/J_{circ}(E) = 1$. This point corresponds to a circular orbit with $r = r_{200}$. Circular orbits of either larger or smaller radius would not be included in our sample as they never cross r_{200}. Hence, $r_{circ}(E)/r_{200}$ either increases or decreases away from unity for increasingly eccentric orbits in our sample. This defines the complicated boundary to the measured bivariate distribution.

The top-right hand panel of Fig. 5 shows the correlated bivariate distribution of radial and tangential velocities. This is similar to that presented and parametrized in Benson (2005). We note that the ridge line of this distribution is approximately circular, i.e. it corresponds to a fixed total velocity $V = \left(V_r^2 + V_\theta^2\right)^{1/2}$.
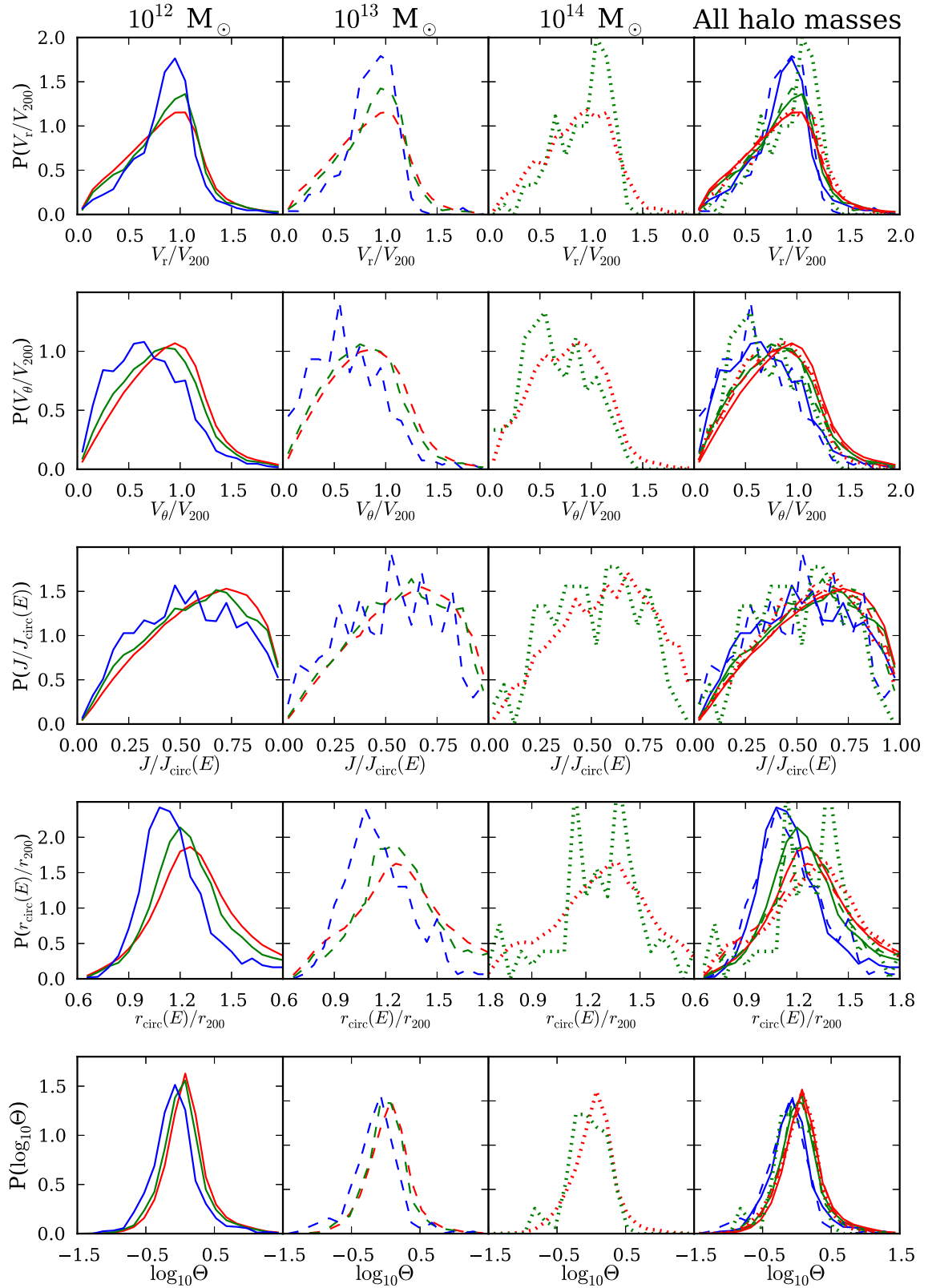
Figure 4. Orbital parameter distributions for bins of different final halo masses and satellite-to-host halo mass ratios, M_s/M_h. The central value of the final halo mass bin is indicated at the top of each column, with the rightmost column overplotting the results from each of the three mass bins using the appropriate line type. The red lines are for $0.0001 < M_s/M_h < 0.005$, green for $0.005 < M_s/M_h < 0.05$ and blue for $M_s/M_h > 0.05$. The first two rows show the radial, V_r/V_{200}, and tangential, V_θ/V_{200}, velocity distributions. The second two rows show the circularity, $J/J_{circ}(E)$, and $r_{circ}(E)/r_{200}$, while the final row shows the distributions of the composite parameter Θ defined in equation (7). Note that for host haloes in the 10^{14} $M_\odot$ bin, we do not show the $M_s/M_h > 0.05$ distributions due to the low number of subhaloes.

Figure 5. The bivariate distributions of orbital parameters for all satellites infalling on to 10^{13} M$_\odot$ haloes. The top panels show the two-dimensional distribution of $r_{\rm circ}(E)/r_{200}$ versus $J/J_{\rm circ}(E)$ and V_θ/V_{200} versus $V_{\rm r}/V_{200}$, respectively. The bottom panels show the two-dimensional distributions of V/V_{200} versus $V_{\rm r}/V_{200}$ and V/V_{200} versus V_θ/V_{200}. The colour bar illustrates the relative density of points (on an arbitrary scale).

The lower two panels of Fig. 5 show the two-dimensional distributions of the total velocity versus either the ratio $V_{\rm r}/V$ or V_θ/V. We see to a good approximation these pairs of parameters appear uncorrelated. This suggests that we can construct a simple model for the full bivariate distribution of orbital parameters by modelling the individual independent distributions of V/V_{200} and $V_{\rm r}/V$. This will then provide a simple parametrized model that can be used in semi-analytic galaxy formation models.

3.4 Fitted distributions

To build a complete model of the bivariate distribution of orbital parameters, we perform fits to the marginalized distributions of both the total velocity, V/V_{200}, and the radial-to-total velocity ratio, $V_{\rm r}/V$. Assuming these to be independent, we can then transform variables to generate model predictions for the distributions of any of the other choices of orbital parameters such as $J/J_{\rm circ}(E)$ and $r_{\rm circ}(E)/r_{200}$. Here, we present these fits as a function of halo mass and satellite-to-halo mass ratio.

The distributions of V/V_{200} for each of our samples are shown in Fig. 6 along with Voigt profile fits. The distributions of V/V_{200} are reasonably symmetric about their means but much more centrally peaked than Gaussians of the same rms width (leptokurtic). We find that the distributions can be fitted well by Voigt profiles, convolutions of a Lorentz profile,
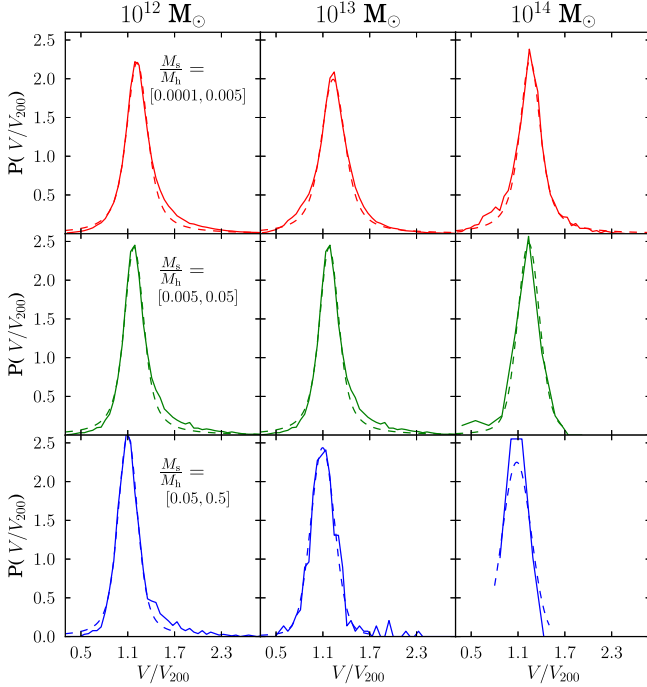
$$P_{\rm L}(x;\gamma) \equiv \frac{\gamma}{\pi(x^2 + \gamma^2)}, \tag{9}$$

and a Gaussian

$$P_{\rm G}(x;\sigma,\mu) \equiv \frac{1}{\sqrt{2\pi}\,\sigma} \exp\left(\frac{-(x-\mu)^2}{2\sigma^2}\right) \tag{10}$$

$$P_{\rm V}(x;\sigma,\gamma,\mu) = \int_{-\infty}^{+\infty} P_{\rm G}(x';\sigma,\mu)P_{\rm L}(x-x';\gamma)\,{\rm d}x', \tag{11}$$

where $x = V/V_{200}$. We determine the best-fitting Voigt profiles by finding the parameters that maximize the likelihood, $\mathcal{L} = \Pi_i P_{\rm V}(x_i;\sigma,\gamma,\mu)$, where the index i runs over all the satellites in the
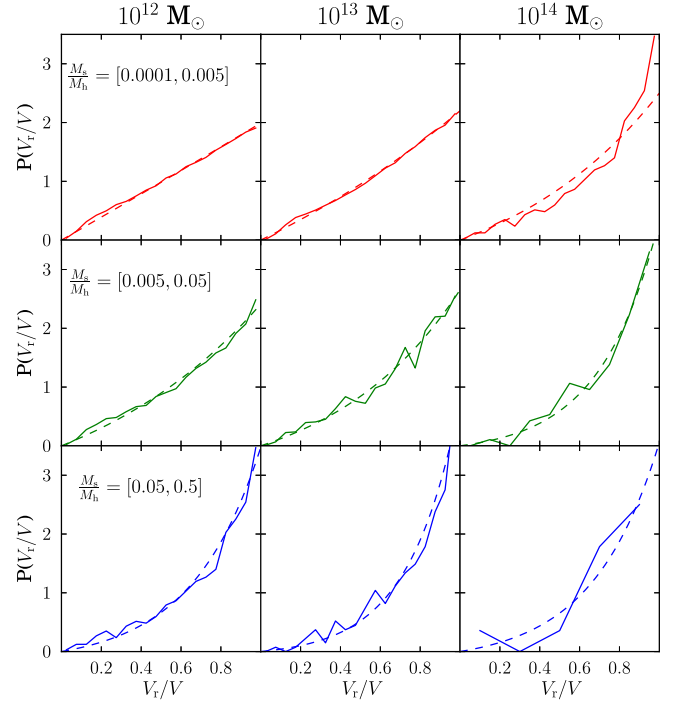
Figure 6. Probability distribution of the total infall velocity, V/V_{200}, as a function of both the satellite-to-host mass ratio at infall and the host halo mass. Each column is for a fixed final halo mass as labelled at the top of the column. Each row is for a different bin in satellite-to-host mass ratio: top (red lines) $0.0001 < M_s/M_h < 0.005$, middle (green lines) $0.005 < M_s/M_h < 0.05$ and bottom (blue lines) $M_s/M_h > 0.05$. The dashed lines are the Voigt profile fits whose parameters, μ, γ and σ are listed in Table 2.
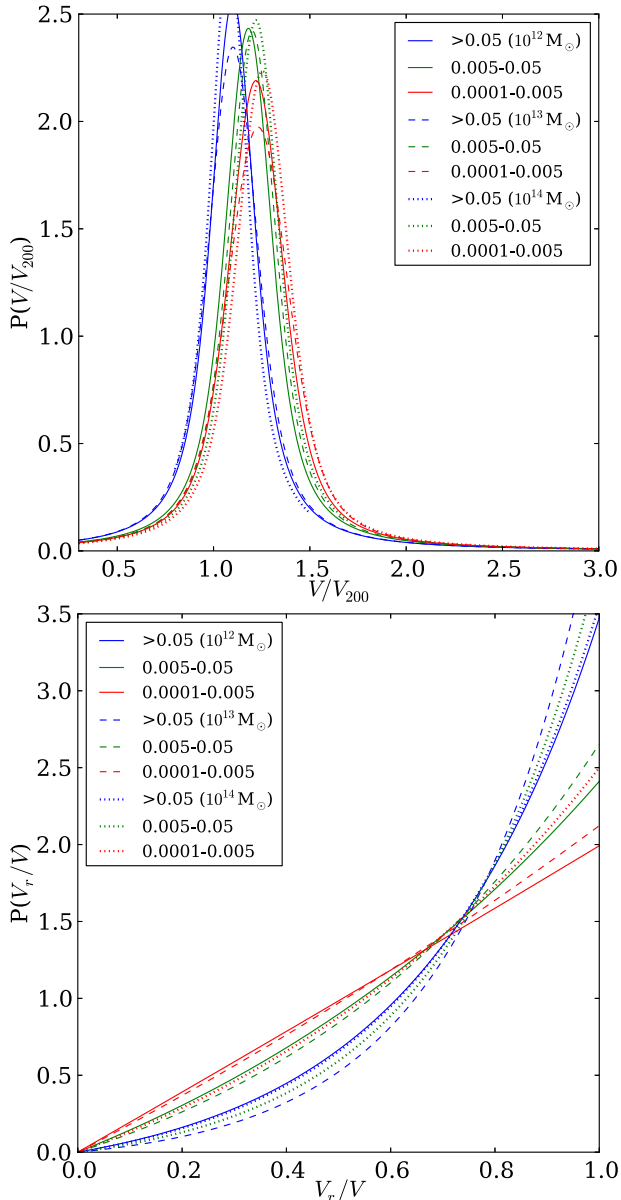
Figure 7. Dependence of the orbital parameters V_r/V on the mass ratio between the satellite halo mass and the host halo mass. Each column is for a fixed final halo mass as labelled at the top of the figure. Each row is for a different bin in satellite-to-host mass ratio, top (red lines) $0.0001 < M_s/M_h < 0.005$, middle (green lines) $0.005 < M_s/M_h < 0.05$ and bottom (blue lines) $M_s/M_h > 0.05$. The dashed curves are the best-fitting exponential distributions and the corresponding value of the parameter B in equation (12) is shown on each panel and in Table 2.

sample. The resulting fits are shown in Fig. 6, and their parameters σ, γ and μ are listed in Table 2.

We find that the distributions V_r/V are well fitted by exponential distributions of the form:

$$P(V_r/V) = A \left(\exp \left(\frac{B V_r}{V} \right) - 1 \right). \qquad (12)$$

Here, A is simply a normalization constant and B is the single free parameter. The distributions of V_r/V and the corresponding maximum likelihood fits are shown in Fig. 7. The distribution is almost linear, $B \ll 1$, for the combination of low M_h and low M_s/M_h. The distributions become increasingly radially biased, peaked at $V_r/V = 1$ (high B), for both increasing M_s/M_h and M_h, consistent with our earlier discussion.

The trends of the distributions of V/V_{200} and V_r/V with halo mass and satellite-to-halo mass ratio are depicted more clearly in Fig. 8, which shows all the fitted distributions on a single panel. In the lower panel, we see the tendency for the distributions to become more radially biased for satellites with higher M_s/M_h. In the upper panel, it is clear that the V/V_{200} distributions have very little dependence on halo mass at fixed M_s/M_h. There is a stronger dependence on M_s/M_h with samples of larger M_s/M_h ratios having narrower distributions and lower mean values. This is consistent with the similar trends in the distribution of $r_{circ}(E)/r_{200}$ that we saw in Fig. 4. These trends can also be seen in Fig. 9, where we plot the dependence of the fit parameters on M_s/M_h. In all halo mass bins the mean, μ, decreases strongly for the highest values of M_s/M_h.

Table 2. Parameters of the fitted orbital parameter distributions for bins of final halo mass, M_h, and the satellite-to-host mass ratio at infall, M_s/M_h. The notation for the parameters of the Voigt and exponential fitting functions are as defined in equations (11) and (12).
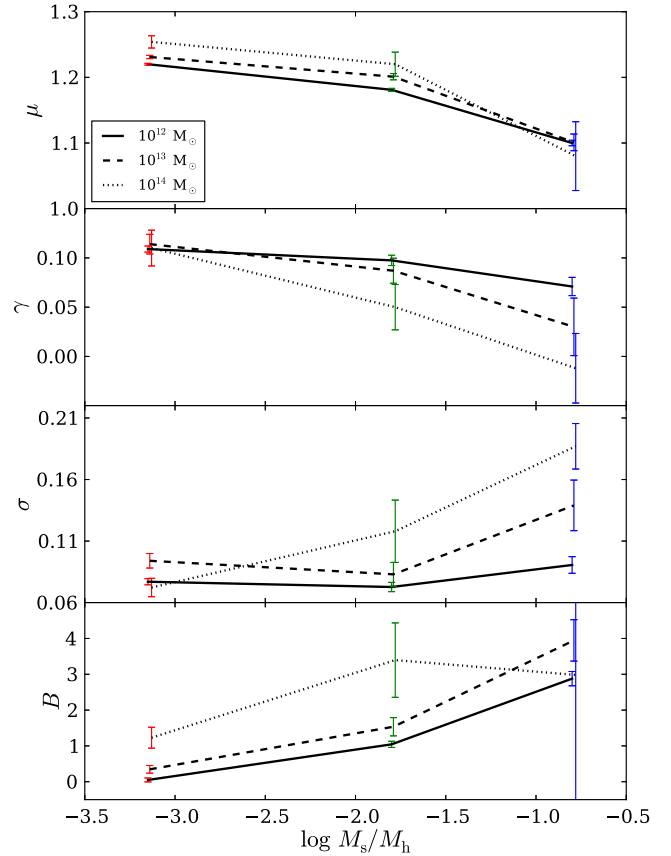
M_h	M_s/M_h	B	γ	σ	μ
10^{12} M$_\odot$	0.0001–0.005	0.049 ± 0.055	0.109 ± 0.003	0.077 ± 0.002	1.220 ± 0.001
10^{13} M$_\odot$	0.0001–0.005	0.548 ± 0.105	0.114 ± 0.010	0.094 ± 0.006	1.231 ± 0.002
10^{14} M$_\odot$	0.0001–0.005	1.229 ± 0.292	0.110 ± 0.018	0.072 ± 0.007	1.254 ± 0.010
10^{12} M$_\odot$	0.005–0.05	1.044 ± 0.086	0.098 ± 0.005	0.073 ± 0.004	1.181 ± 0.002
10^{13} M$_\odot$	0.005–0.05	1.535 ± 0.255	0.087 ± 0.013	0.083 ± 0.010	1.201 ± 0.005
10^{14} M$_\odot$	0.005–0.05	3.396 ± 1.040	0.050 ± 0.023	0.118 ± 0.025	1.236 ± 0.020
10^{12} M$_\odot$	0.05–0.5	2.878 ± 0.200	0.071 ± 0.010	0.091 ± 0.007	1.100 ± 0.004
10^{13} M$_\odot$	0.05–0.5	3.946 ± 0.578	0.030 ± 0.030	0.139 ± 0.021	1.100 ± 0.013
10^{14} M$_\odot$	0.05–0.5	2.982 ± 4.646	-0.012 ± 0.035	0.187 ± 0.019	1.084 ± 0.052

Figure 9. Dependence of fitting parameters μ, γ, σ and B on the satellite-to-host mass ratio at infall. The different line styles denote different host halo masses, as indicated in the legend. The colours of the error bars denote satellite-to-host mass ratio bins: red $0.0001 < M_\mathrm{s}/M_\mathrm{h} < 0.005$, green $0.005 < M_\mathrm{s}/M_\mathrm{h} < 0.05$ and blue $M_\mathrm{s}/M_\mathrm{h} > 0.05$. The errors are estimated by bootstrap sampling of the $z = 0$ halo catalogue.

Figure 8. The fitted distributions of the orbital parameters V/V_{200} (top) and V_r/V (bottom) for the different values of both the satellite-to-host mass ratio and the host halo mass. Line colour denotes satellite-to-host mass ratio, red $0.0001 < M_\mathrm{s}/M_\mathrm{h} < 0.005$, green $0.005 < M_\mathrm{s}/M_\mathrm{h} < 0.05$ and blue $M_\mathrm{s}/M_\mathrm{h} > 0.05$. The line style indicates the host halo mass, solid $10^{12}\,\mathrm{M}_\odot$, dashed $10^{13}\,\mathrm{M}_\odot$ and dotted $10^{14}\,\mathrm{M}_\odot$.
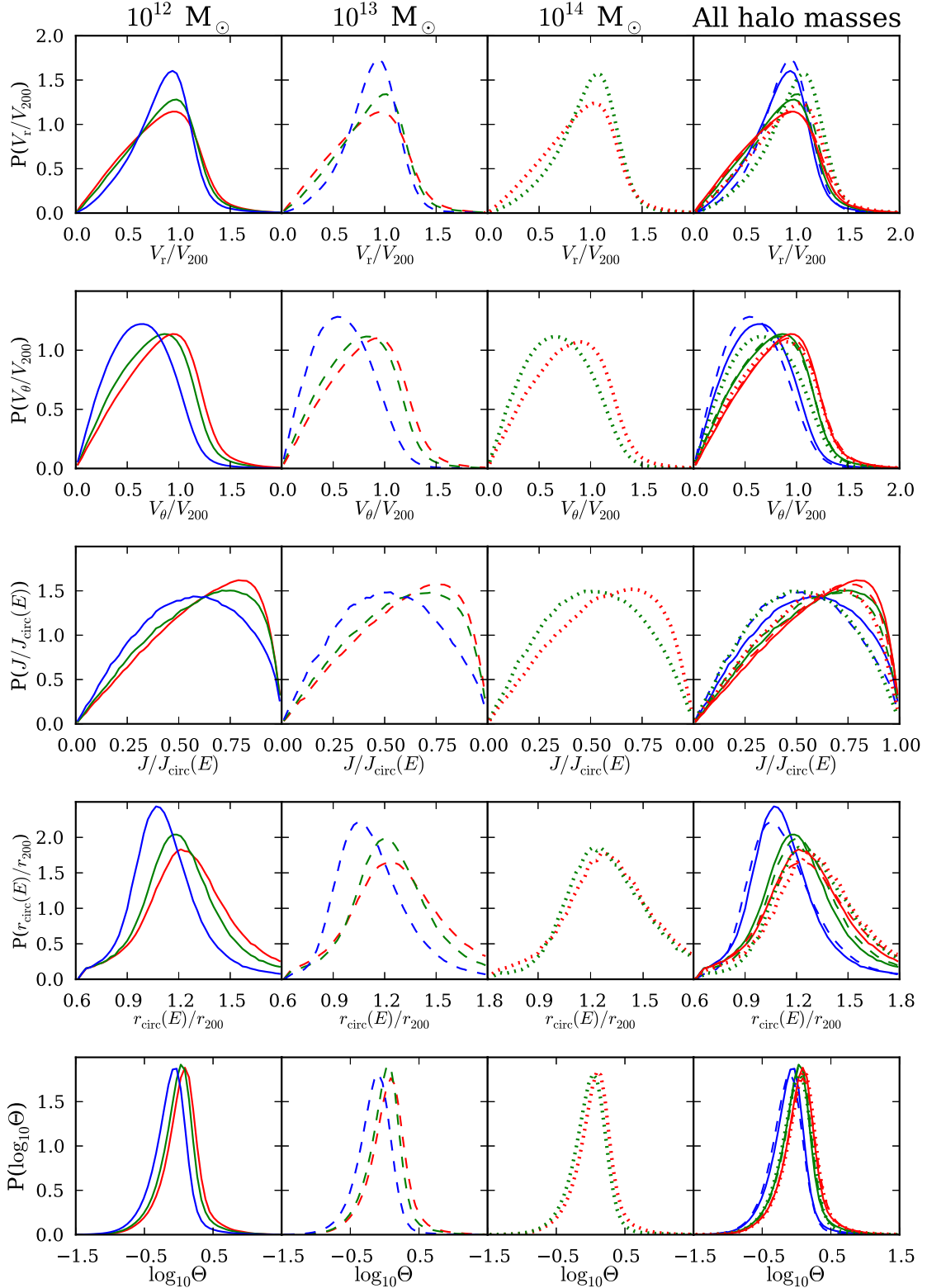
3.5 Derived distributions

If the fits we have presented in Section 3.4 are accurate and if V_r/V and V/V_{200} are uncorrelated, then we can use these distributions to derive model distributions of any other choice of orbital parameter. For instance, we can select pairs of values of V_r/V and V/V_{200} from the fitted distributions and compute the radial and tangential velocities using

$$\frac{V_\mathrm{r}}{V_{200}} = \left(\frac{V_\mathrm{r}}{V} \right) \left(\frac{V}{V_{200}} \right) \qquad (13)$$

and

$$\frac{V_\theta}{V_{200}} = \left(\frac{V}{V_{200}} \right) \sqrt{1 - \left(\frac{V_\mathrm{r}}{V} \right)^2}. \qquad (14)$$

We can also derive $J/J_\mathrm{circ}(E)$, $r_\mathrm{circ}(E)/r_{200}$ and Θ from V_r/V and V/V_{200} using the equations in Section 2.2. We show all the resulting orbital parameter distributions in Fig. 10, which should be compared with Fig. 4. Direct comparison of the two figures shows that these are faithful representations of the data and validate the assumption that, to a good approximation, V_r/V and V/V_{200} can be treated as independent random variables. The model distributions shown in Fig. 10, particularly the superimposed distributions in the right-hand column, clearly show both the strong dependence on $M_\mathrm{s}/M_\mathrm{h}$ and the much weaker dependence on M_h.

The narrower width of the V/V_{200} distributions for high $M_\mathrm{s}/M_\mathrm{h}$, which we see in Fig. 8, is reflected in a decreasing value of γ (the width of the Lorentzian) with increasing $M_\mathrm{s}/M_\mathrm{h}$, which has greater effect on the width of the distribution than the corresponding slow increase in σ (the width of the Gaussian). The error bars shown on Fig. 9 have been estimated by bootstrap resampling of the $z = 0$ halo catalogue, and we have investigated the correlations of all the pairs of parameters. The only significant correlation we find is an anticorrelation between σ and γ. This is to be expected as the overall width of the distribution is determined by $\sigma^2 + \gamma^2$, while their ratio, γ/σ, determines how peaked the distribution is (its kurtosis).

Figure 10. Like Fig. 4, but showing the distributions derived from the fits presented in Section 3.4 rather than the directly measured distributions.

The values of V and V_r are directly measured and so the fitted distributions of V_r/V and V/V_{200} make no assumption about the form of the density profile of the host halo. Hence, if preferred one can compute the corresponding orbital parameters $r_{\rm circ}(E)/r_{200}$ and $J/J_{\rm circ}(E)$ using an NFW model of the halo profile. Following the same steps as outlined in Section 2.2, but for an NFW profile, one can show that, $r_{\rm circ}(E)/r_{200}$ can be evaluated by solving

$$\frac{r_{\rm circ}(E)}{r_{200}} = \frac{2\ln(1 + c\,r_{\rm circ}(E)/r_{200}) - 1/f(c\,r_{\rm circ}(E)/r_{200})}{2\ln(1+c) - V^2/(V_{200}^2 f(c))}, \quad (15)$$
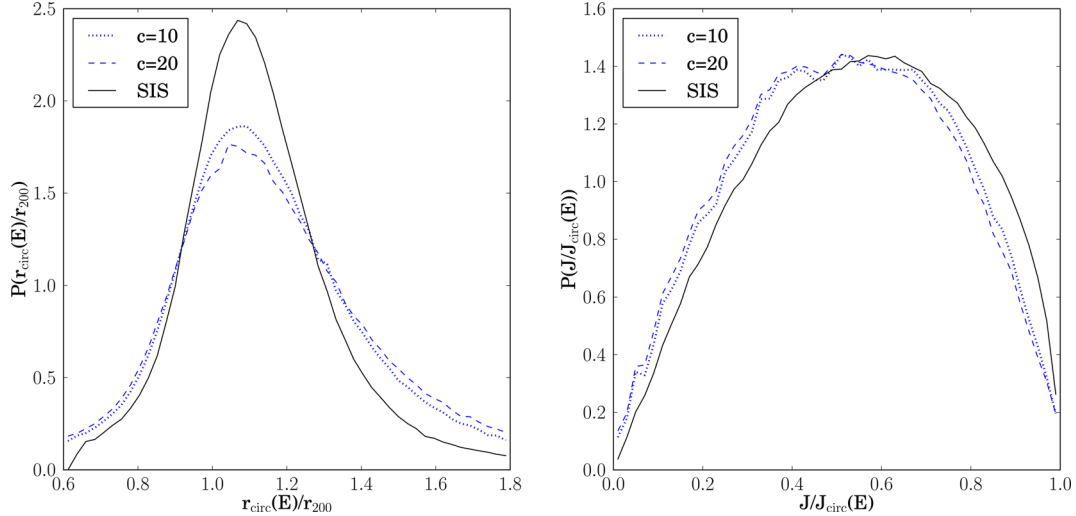
Figure 11. Comparison of the fitted distributions of orbital parameters $r_{circ}(E)/r_{200}$, $J/J_{circ}(E)$ for different assumed host halo density profiles. The black solid curve is for the default SIS profile when the blue dotted and dashed curves are for NFW profiles with concentrations $c = 10$ and 20, respectively. This example is for host halo mass $M_h = 10^{12}$ M$_\odot$ and satellite to mass ratio in the range $0.05 < M_s/M_h < 0.5$.

where $f(c) = 1/(\ln(1 + c) - c/(c + 1))$ and c is the concentration.[2] Having found $r_{circ}(E)/r_{200}$, $J/J_{circ}(E)$ can be found using

$$\frac{J}{J_{circ}(E)} = \frac{V_\theta}{V_{200}} \left(\frac{f(c\, r_{circ}(E)/r_{200})}{f(c)} \right)^{1/2} \left(\frac{r_{circ}(E)}{r_{200}} \right)^{-1/2}. \quad (16)$$

As an example, Fig. 11 compares the resulting distributions of $r_{circ}(E)/r_{200}$ and $J/J_{circ}(E)$ for host halo mass $M_h = 10^{12}$ M$_\odot$ and satellite to mass ratio in the range $0.05 < M_s/M_h < 0.5$. The NFW distributions of $r_{circ}(E)/r_{200}$ are broader than the corresponding SIS distribution as over the relevant range $r_{circ}(E)$ is a stronger function of energy in the NFW case than it is in the SIS case. The energy of a circular orbit at $r = r_{200}$ is the same for both NFW and SIS as both profiles are normalized to enclose the same mass, M_{200}, at this radius. As the orbital energy is increased $r_{circ}(E)$ will grow faster for the NFW case as it has a more rapidly decreasing density profile. This leads to the enhanced tail of orbits with large $r_{circ}(E)/r_{200}$. Higher concentration steepens the density profile around r_{200} and so further enhances this tail, but this is a very weak effect. The J/J_{circ} distributions for the NFW models are slightly shifted to lower values. Since the measured values of J do not depend on the model, this shift is caused by the typical values of J_{circ} being larger in the NFW case. For a circular orbit at r_{200} the NFW and SIS models have identical J_{circ} while at larger radii J_{circ} for an NFW profile exceeds that for a SIS. Hence, the small shift to lower J/J_{circ} is a result of this sample having a median value of $r_{circ}(E)/r_{200}$ greater than unity. The shift is larger for lower mass satellites as their distributions of $r_{circ}(E)/r_{200}$ have larger median values. The dependence on concentration is again very weak.

4 CONCLUSIONS

We have employed the DOVE high-resolution cosmological *N*-body simulation with more than 4 billion particles to study the distribution of the orbits of infalling satellites during hierarchical halo

formation in the standard ΛCDM cosmology. We study host haloes with masses from 10^{12} to 10^{14} M$_\odot$ and satellites with masses as low as 2×10^8 M$_\odot$. Compared to previous studies (Tormen 1997; Vitvitska et al. 2002; Benson 2005; Wetzel 2011), we have better mass and time resolution and a larger sample of satellite orbits.

There are various choices for the pair of orbital parameters that specify a satellite orbit in a spherical potential. We quantify the distributions of the radial, V_r, and tangential, V_θ, velocities as well as other common alternatives such as the circularity, $J/J_{circ}(E)$ and the radius of the circular orbit of the same energy, $r_{circ}(E)$.

We have examined the dependence of the distributions of these orbital parameters on both the host halo mass, M_h, and the mass ratio between the satellite and host, M_s/M_h. We find that the strongest trends are with M_s/M_h at fixed M_h. Satellites with larger M_s/M_h tend to be on more radial orbits with lower angular momentum and are more tightly bound. At fixed M_s/M_h there is a trend for satellites around more massive haloes to also be on more radial orbits, but this trend is weaker. In so far as previous authors have examined similar relationships, our results are consistent with their data. However, while Wetzel (2011) had not detected a significant dependence of orbital parameters on satellite mass ratio, possibly due to their limited sample size, our larger sample of orbits reveals a dependence, particularly at high mass ratios.

In general, we find that complementary pairs of orbital parameters, such as (V_r, V_θ), are non-trivially correlated, making a complete description of their bivariate distribution complex. However, we find that, to a good approximation, the distributions of total infall velocity $V = (V_r^2 + V_\theta^2)^{1/2}$ and the ratio V_r/V are uncorrelated. We present accurate Voigt and exponential fits to their respective distributions. Assuming them to be uncorrelated, we transform these simple bivariate distributions and demonstrate that the distributions of other choices of orbital parameter can be successfully recovered.

---

[2] This equation can be solved iteratively by starting with the guess $r_{circ}(E)/r_{200} = 1$ and obtaining the next iteration by substituting into the RHS.

REFERENCES

Baugh C. M., 2006, Rep. Prog. Phys., 69, 3101
Benson A. J., 2005, MNRAS, 358, 551
Binney J., Tremaine S., 2008, Galactic Dynamics, 2nd edn. Princeton Univ. Press, Princeton, NJ
Boylan-Kolchin M., Ma C.-P., Quataert E., 2008, MNRAS, 383, 93
Chandrasekhar S., 1943, ApJ, 97, 255
Cole S., Lacey C., 1996, MNRAS, 281, 716
Davis M., Efstathiou G., Frenk C. S., White S. D. M., 1985, ApJ, 292, 371
Gill S. P. D., Knebe A., Gibson B. K., Dopita M. A., 2004, MNRAS, 351, 410
Jenkins A., 2010, MNRAS, 403, 1859
Jenkins A., 2013, MNRAS, 434, 2094
Jiang C. Y., Jing Y. P., Faltenbacher A., Lin W. P., Li C., 2008, ApJ, 675, 1095
Jiang L., Helly J. C., Cole S., Frenk C. S., 2014, MNRAS, 440, 2115
Khochfar S., Burkert A., 2006, A&A, 445, 403
Klypin A., Gottlöber S., Kravtsov A. V., Khokhlov A. M., 1999, ApJ, 516, 530
Komatsu E. et al., 2011, ApJS, 192, 18
Lacey C., Cole S., 1993, MNRAS, 262, 627
Libeskind N. I., Frenk C. S., Cole S., Helly J. C., Jenkins A., Navarro J. F., Power C., 2005, MNRAS, 363, 146
Moore B., Ghigna S., Governato F., Lake G., Quinn T., Stadel J., Tozzi P., 1999, ApJ, 524, L19
Navarro J. F., Frenk C. S., White S. D. M., 1996, ApJ, 462, 563
Schaye J. et al., 2014, preprint (arXiv:e-prints)
Springel V., 2005, MNRAS, 364, 1105
Springel V., White S. D. M., Tormen G., Kauffmann G., 2001, MNRAS, 328, 726
Tormen G., 1997, MNRAS, 290, 411
Vitvitska M., Klypin A. A., Kravtsov A. V., Wechsler R. H., Primack J. R., Bullock J. S., 2002, ApJ, 581, 799
Wang H. Y., Jing Y. P., Mao S., Kang X., 2005, MNRAS, 364, 424
Wetzel A. R., 2011, MNRAS, 412, 49
White S. D. M., Rees M. J., 1978, MNRAS, 183, 341
Zentner A. R., Berlind A. A., Bullock J. S., Kravtsov A. V., Wechsler R. H., 2005, ApJ, 624, 505

APPENDIX A: CIRCULARITY IN THE KEPLERIAN APPROXIMATION

To compare the circularity, $J/J_{circ}(E)$, inferred under the assumption that the infalling satellite, and host halo are treated as two point masses on a Keplerian orbit with the SIS model; we need to compare the corresponding expressions for the angular momenta of circular orbits, $J_{circ}(E)$. For the Keplerian case, this is easily derived from the angular momentum of a circular orbit of radius r, $J_{circ} = \mu V_{circ} r$, where the circular velocity at separation r is given by $\mu V_{circ}^2 = GM_h M_s/r$ and the corresponding orbital energy $E = \mu V_{circ}^2/2 - GM_h M_s/r$. Here μ is the reduced mass, which can be expressed in terms of the satellite and host masses as $\mu = M_s M_h/(M_s + M_h)$.
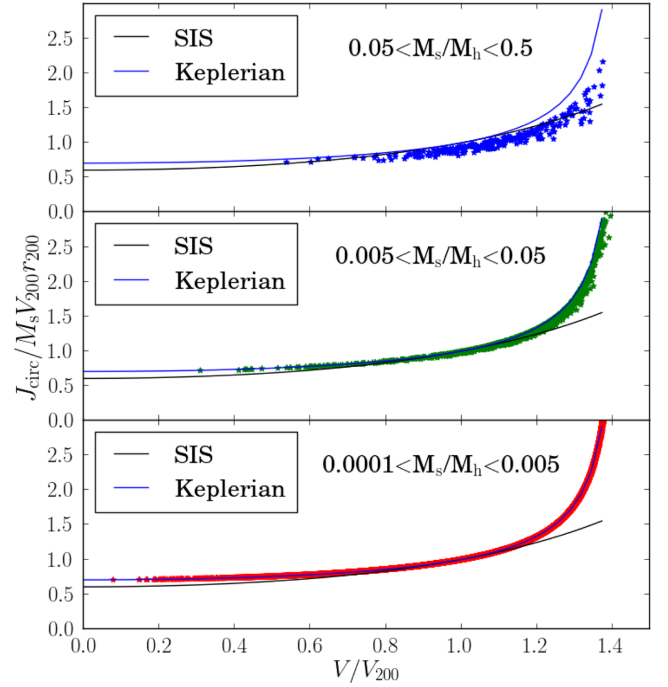
Figure A1. A comparison of the Keplerian and SIS models of J_{circ} in units of $M_s V_{200} r_{200}$ for satellites with infall velocity, V, at the virial radius r_{200}. In each panel, the black solid line is the SIS expression, and the blue solid line is for the Keplerian case in the limit $M_s/M_h \ll 1$. The stars show the result of the full Keplerian expression including the dependence on the reduced mass, μ, for samples of satellites in different bins of M_s/M_h.

Eliminating both V_{circ} and r from these three equations yields

$$J_{circ}^{Kep}(E) = \sqrt{\frac{(GM_h M_s)^2 \mu}{-2E}}. \tag{A1}$$

If V is the velocity difference between the satellite and host when the satellite crosses the virial radius, r_{200}, then

$$E = \frac{1}{2}\mu V^2 - \frac{GM_s M_h}{r_{200}} = \frac{1}{2}\mu V^2 - M_s V_{200}^2, \tag{A2}$$

where the circular velocity, V_{200}, is given by $V_{200} = \sqrt{GM_h/r_{200}}$. Using equation (A2) to substitute for E in equation (A1) yields
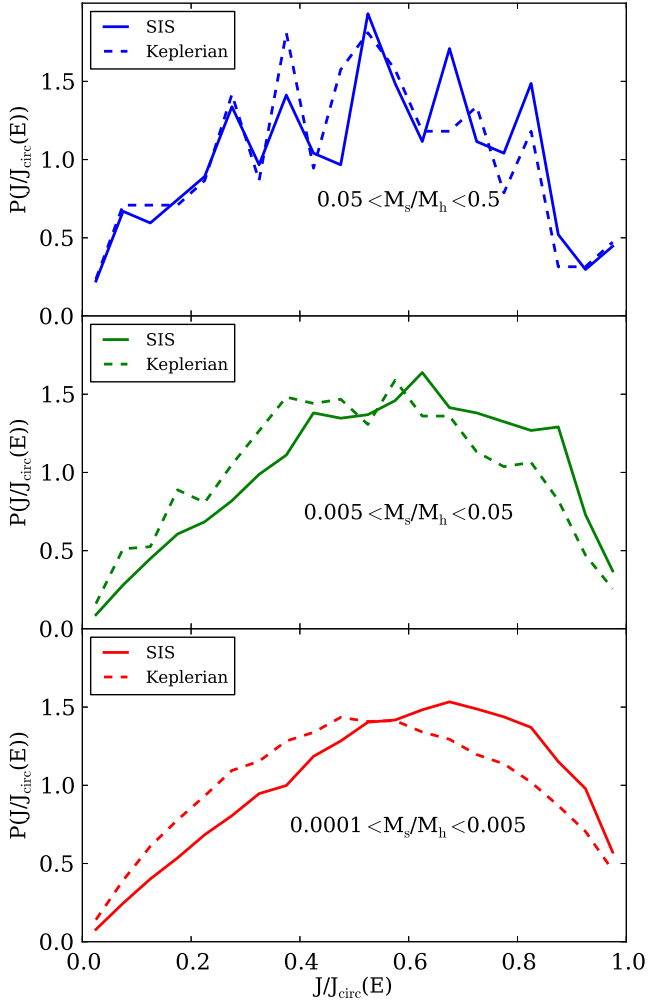
$$\frac{J_{circ}^{Kep}(E)}{M_s V_{200} r_{200}} = \frac{1}{\sqrt{2M_s/\mu - V^2/V_{200}^2}}. \tag{A3}$$

This compares with the SIS expression for J_{circ} derived in Section 2.2,

$$\frac{J_{circ}^{SIS}(E)}{M_s V_{200} r_{200}} = \exp\left(\frac{1}{2}\left(\frac{V^2}{V_{200}^2} - 1\right)\right). \tag{A4}$$

The solid curves in Fig. A1 compare, as a function of satellite infall velocity, V, the SIS expression with the Keplerian expression evaluated in the limit $M_s/M_h \ll 1$, such that $\mu \to M_s$. The individual points on the different panels show the results of the full Keplerian expression with its dependence on M_s/μ applied to our satellite sample in different bins of M_s/M_h. The model curves necessarily agree at $V = V_{200}$ because the mass enclosed in a circular orbit at r_{200}, where the circular velocity is V_{200}, is the same by construction. For $M_s/M_h \ll 1$, the difference between the two models is largest at large V/V_{200} where the orbits extend far beyond r_{200} and hence

the mass enclosed in the SIS greatly exceeds the mass assumed in the point mass approximation. The effect of the reduced mass, μ, is small for $M_s/M_h < 0.05$, but for $0.05 < M_s/M_h < 0.5$ it has the effect of reducing $J_{\rm circ}^{\rm Kep}(E)$ and produces values closer to the SIS case. This is demonstrated in Fig. A2 which compares the distribution of circularities, $J/J_{\rm circ}(E)$, evaluated using the two different expressions for three ranges in satellite-to-host mass ratio. Overall, the two models agree well with each other for higher values of M_s/M_h, but they differ for the lowest mass ratio bins.

Figure A2. Distributions of circularity, $J/J_{\rm circ}(E)$, for infalling satellite haloes for host haloes in a mass bin centred on 10^{13} M$_\odot$. Solid curves show the distribution derived assuming that a SIS and dashed curves show the distribution derived using the Keplerian model. The three panels are for the same three bins of M_s/M_h as in Fig. A1.

This paper has been typeset from a TEX/LATEX file prepared by the author.